One dimensional imager of neutrons on the Z machine

David J. Ampleford, Carlos L. Ruiz, David N. Fittinghoff, Jeremy D. Vaughan, Kelly Hahn, Brandon Lahmann, Maria Gatu-Johnson, Johan Frenje, Richard Petrasso, Christopher R. Ball, Andrew J. Maurer, Patrick F. Knapp, Adam J. Harvey-Thompson, John Fisher, Perry Alberto, Jose A. Torres, Gary Cooper, Brent Jones, Gregory A. Rochau, and Mark J. May

One dimensional imager of neutrons on the Z machine

David J. Ampleford,[1,a)] Carlos L. Ruiz,[1] David N. Fittinghoff,[2] Jeremy D. Vaughan,[1,3]
Kelly Hahn,[1] Brandon Lahmann,[4] Maria Gatu-Johnson,[4] Johan Frenje,[4] Richard Petrasso,[4]
Christopher R. Ball,[1] Andrew J. Maurer,[1] Patrick F. Knapp,[1] Adam J. Harvey-Thompson,[1]
John Fisher,[1] Perry Alberto,[1] Jose A. Torres,[1] Gary Cooper,[3] Brent Jones,[1]
Gregory A. Rochau,[1] and Mark J. May[2]

[1]*Sandia National Laboratories, Albuquerque, New Mexico 87185, USA*
[2]*Lawrence Livermore National Laboratory, Livermore, California 94550, USA*
[3]*University of New Mexico, Albuquerque, New Mexico 87131, USA*
[4]*Massachusetts Institute of Technology, Cambridge, Massachusetts 02139, USA*

We recently developed a one-dimensional imager of neutrons on the Z facility. The instrument is designed for Magnetized Liner Inertial Fusion (MagLIF) experiments, which produce D-D neutrons yields of $\sim 3 \times 10^{12}$. X-ray imaging indicates that the MagLIF stagnation region is a 10-mm long, ~ 100-μm diameter column. The small radial extents and present yields precluded useful radial resolution, so a one-dimensional imager was developed. The imaging component is a 100-mm thick tungsten slit; a rolled-edge slit limits variations in the acceptance angle along the source. CR39 was chosen as a detector due to its negligible sensitivity to the bright x-ray environment in Z. A layer of high density poly-ethylene is used to enhance the sensitivity of CR39. We present data from fielding the instrument on Z, demonstrating reliable imaging and track densities consistent with diagnosed yields. For yields $\sim 3 \times 10^{12}$, we obtain resolutions of ~ 500 μm. *Published by AIP Publishing.*
https://doi.org/10.1063/1.5038118

I. INTRODUCTION

Neutron imaging has demonstrated a significant impact on the understanding of Inertial Confinement Fusion (ICF) plasmas and in constraining simulations of such plasmas. On the National Ignition Facility (NIF), two-dimensional neutron imaging has been developed using thick pinhole and penumbral-aperture imaging techniques[1] and has led to significant new insights into stagnation physics.[2] For magneto-inertial fusion, and specifically Magnetized Liner Inertial Fusion (MagLIF)[3] on the Z machine at Sandia National Laboratories, neutron imaging provides a very specific insight into the stagnation plasma. As a laser is used to preheat the fuel through a thin CH window at one end of the target, the presence of low-Z window mix is expected to vary along the stagnation column[4]—a comparison between the local x-ray and neutron emissivity of the hot fuel is one approach to providing a local measure of this mix. Also, diagnosing the magnetization of the stagnation column is a key to demonstrating magnetic flux compression, which is key to MagLIF. Recent work has developed techniques using the yield and spectrum of secondary D-T reactions within the D-D plasma;[5] a key assumption in that work is that there is a continuous column of D-D-producing plasma, and experimental verification of this assumption through neutron imaging would be valuable.

Neutron imaging of MagLIF plasmas presents a unique set of challenges. Due to the 2D convergent geometry, the plasma stagnation, and hence neutron production, is expected from a long (~ 10 mm) narrow (<100 μm diameter) column.[6] Present yield levels from D-D experiments on Z are $\sim 3 \times 10^{12}$, limiting what can be achieved with pinhole imaging; however, a one-dimensional slit image is more achievable. Previously, various neutron imagers designed for one-dimensional imaging have been proposed for Z; however, these designs were either not built or proved difficult to field in the Z environment.[7,8] Further constraining the design of such an instrument is the large x-ray and Bremsstrahlung background on Z, which can lead to challenges in data recording with any detector that has a sensitivity to x-ray photons.

In this paper, we present the design, expected performance, initial data, and data analysis of a new One-Dimensional Imager of Neutrons, ODIN, on the Z facility. ODIN is aimed at providing 500 μm axial resolution over the 10-mm load height with a good signal-to-noise ratio and background for the current D-D neutron yields from MagLIF.

II. INSTRUMENT DESIGN

A. Overview

ODIN uses an extended, rolled-edge slit to produce a one-dimensional image of the D-D neutrons from an extended source onto plates of CR39, which are used as the detector. The slit center is positioned 220 mm from the object (the target in the Z chamber), and the principle detector location is 795 mm
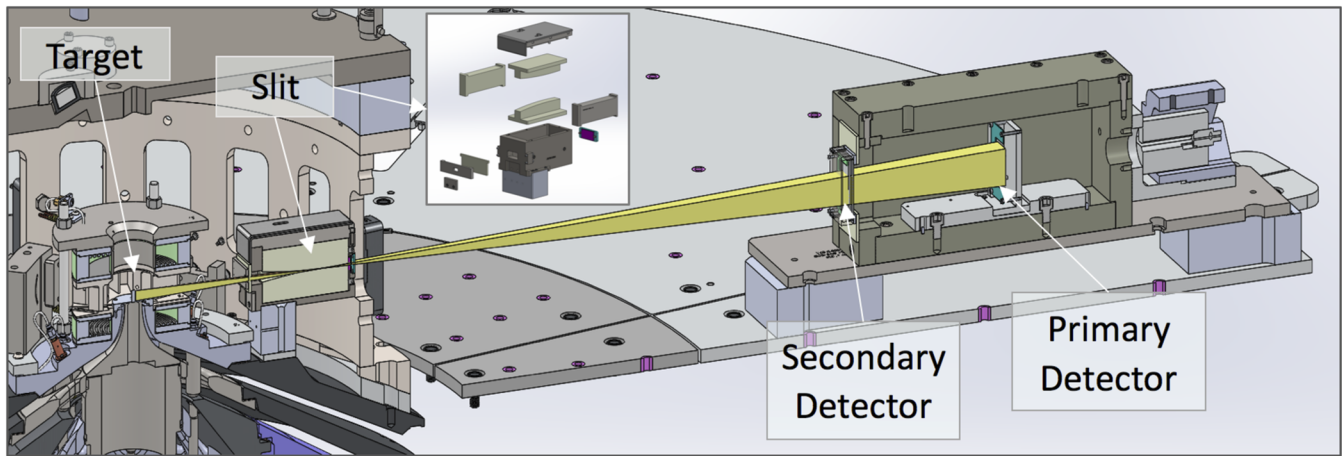
FIG. 1. Summary of ODIN. The target is to the left of the image. Shown in yellow is a ray trace from the target, through the rolled edge slits, to the detector housing at the right of the image. An exploded view of the slit assembly is shown. Primary and secondary detector locations are shown.

from the slit, providing a magnification of 3.6. An overview of the instrument is shown in Fig. 1. The entire instrument sits within the Z-machine's vacuum chamber, with the slit assembly attached to part of the final power flow hardware, and the detector assembly positioned on the *work platform* above the magnetically insulated transmission lines of the machine.

B. Slit design

The imaging element of ODIN is a horizontal slit. Tungsten, with a mean free path for D-D neutrons of $\lambda_{\text{D-D}} = 21.9$ mm,[9] is used for the slit. The use of a high-Z slit material minimizes small-angle scattering. To provide sufficient contrast, an extended slit with a 100-mm thickness is used; the full depth of the slit provides a contrast 1×10^{-2} compared to unobscured trajectories. Typically, extended slits (or extended pinholes) suffer considerably from vignetting, which leads to large gradients in throughput across the image plane and significantly limits the field of view.[10] To minimize this effect, a rolled edge slit design was used, as shown in the exploded view in the inset in Fig. 1. The aim of the rolled edge slit is to achieve an open slit over the full imaging height while maximizing the depth of tungsten for neutron trajectories away from the intended trajectory. Here, to determine the radius of curvature needed in the rolled edge, we treat the slit as perfectly attenuating to neutrons (a more detailed discussion of the effect of neutron trajectories through the slit is provided in a Sec. III). For the radius of curvature R, the effective opening h_{eff} of a slit spaced h_{slit} with the apex (narrowest section) for a neutron path entering the slit at angle θ is $h_{eff} = h_{slit} - R(1 - \cos\theta)$. Given that the source is located D_{slit} from the slit, for a ray that originated from axial position y on the target, we find

$$h_{eff} = h_{slit} - R \frac{\left(1 - \left(1 - \frac{y}{D_{slit}}\right)^2\right)}{2}. \tag{1}$$

The apex of the slit was located $D_{slit} = 220$ mm from the source—this is a location known to have manageable debris from the Z load.

In general, the smaller the radius of curvature, the larger the field of view that can be imaged but with the sacrifice of an increased background. The radius of curvature of the rolled edge was chosen to be 500 mm—at the chosen fielding distance, a 250 μm slit is *fully open* for ±5 mm in the object plane, allowing imaging over the full height of a 10-mm tall target while maximizing the tungsten thickness. Transmission of neutrons through the rolled edge leads to a larger effective opening, impacting both resolution and throughput—a detailed calculation of the expected operation is included in Sec. III.

Simple geometric calculations of the slit area (250 μm height, 12 mm width) indicate that the collection solid angle is 6.2×10^{-5} sr, or a collection efficiency of ~5×10^{-6} of the source neutrons (1.5×10^7 neutrons pass through the slit for a nominal 3×10^{12} source). The slit is assembled in four pieces—two rolled W edges and two spacers. Slit spacers were fabricated to 250, 500, and 750 μm openings (the as-fabricated slit openings are 266, ~500, and 863 μm, respectively). The tungsten rolled edge is common to each slit spacing.

C. Detector design

In the bright x-ray environment on Z, a detector with low response to x-rays was needed. As such, CR39 was chosen as the primary detector. Neutrons incident on CR39 produce recoil protons that produce detectable tracks in CR39 after chemical etching.[11] CR39 has been demonstrated to have a negligible response to photons,[12] and any tracks produced via the photon interaction are distinguishable from those produced by neutrons in the image processing steps used. For D-D neutrons, the quantum efficiency of CR39 is 1.1×10^{-4} tracks per incident neutrons.[11–13] To enhance the response to D-D neutrons, a 1 mm thick layer of high density polyethylene (HDPE) was positioned ahead of CR39. Incident neutrons interact with the HDPE producing a proton, which has a much higher efficiency than neutrons in CR39. Using the HDPE provides a factor of ~8 enhancement of tracks to the efficiency of neutrons incident on the bare CR39.[14]

The CR39 plates are positioned 1015 mm from the source (the *primary* CR39 location), providing a magnification of 3.6.

Assuming 1.5×10^7 neutrons are incident on the HDPE-CR39 pair (see discussion in Sec. II B), we expected ~1.3×10^4 tracks on CR39, or ~650 tracks/cm^2 for a uniformly emitting source. This track density is relatively low given a background track density of 1500 tracks/cm^2, but given the ability to average over large regions of the detector, it was expected to be measurable. Centering pins are used in the detector assembly to provide accurate placement of CR39 within the instrument, to establish the orientation of the scanned CR39, and to give cross-registration between detector layers. Several HDPE-CR39 pairs are fielded within this primary detector location, with the aim of summing/averaging across layers to improve statistics.

The detector assembly is shown to the right of Fig. 1. The main detector location is at the center of the housing. An additional CR39-HDPE pair is placed at the front of the detector housing (to the left of the detector housing in Fig. 1). This provides a higher track density but a lower magnification CR39 location. The purpose of this is two-fold—the higher expected track density is useful for lower yield experiments, and if the two CR39 locations each have data, it provides a useful check that the instrument is performing as designed (scattered neutrons will not produce identical false images at two locations).

III. PERFORMANCE ESTIMATES

In this section, we estimate the integrated performance of the instrument. Specifically, transmission through the W slit impacts both the resolution and throughput of the instrument, so it is intrinsic to unfolding data. Here we consider geometric effects, including transmission through the W slit; scattering effects are not included.

First, we can estimate the clear opening of the source, as is shown in Eq. (1). Additionally, based on the cylindrical profile of the slit (see Fig. 2), we can calculate the path length through the slit for positions outside this clear opening. In the plane of the slit, we can relate the path length, d, to the radius of curvature of the slit R and to the position of the path relative to the center of the slit curvature, a, and (all of which are defined in Fig. 2)

$$R^2 = a^2 + \left(\frac{d}{2}\right)^2. \tag{2}$$

Substituting for the position trajectory relative to the slit center, $\Delta y'' = R - a$, and incorporating the the effective slit opening h_{eff} from (1) we find:
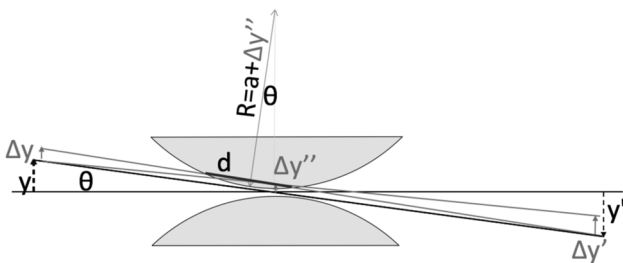
FIG. 2. Geometry used for throughput and resolution calculations.

$$d = 2\sqrt{R^2 - \left(R - \left(\Delta y'' - \frac{h_{eff}}{2}\right)\right)^2}. \tag{3}$$

This relationship relates the path length through the W slit to the position relative to the slit opening. To translate from the slit plane to the image plane, it is necessary to scale to $\Delta y' = (M + 1)\,\Delta y''$ (see Fig. 2). Similarly, to translate from the slit plane to the object place, we scale to $\Delta y = (M + 1)\,\Delta y''/M$. From the calculated path lengths and the known mean free path, λ, we can calculate the expected transmission of the slit for arbitrary rays and therefore the line spread function,

$$
\begin{aligned}
&\text{If } \Delta y'' > \frac{h_{eff}}{2} \qquad T = e^{-\frac{d}{\lambda}},\\
&\text{If } \Delta y'' < \frac{h_{eff}}{2} \qquad T = 1.
\end{aligned}
\tag{4}
$$

Here we ignore scattering effects—MCNP calculations of scattering are underway.[15]

Figure 3(a) shows the line spread functions in the image plane for a set of point sources separated by 0.5 mm through the 10-mm field of view and a 266 μm slit. The flat top of each line spread function represents the open region of the slit. Beyond the opening, there is a wide tail due to transmission through the W slit material. Notably, for the rolled edge slit, the function of the line spread function due to transmission through the W slit does not vary with height; the only variation is in the width of the flat-top of the profile from the open section of the slit.

The line spread functions are used to evaluate the resolution of the instrument. The full width at half maximum of the line spread function is often used to evaluate the resolution and is shown blue line in Fig. 3(b). Given that the shape of the line spread function varies for the different parts of the image, it can be more informative to consider where most of the transmitted fluence is. As such, in Fig. 3(b), we also
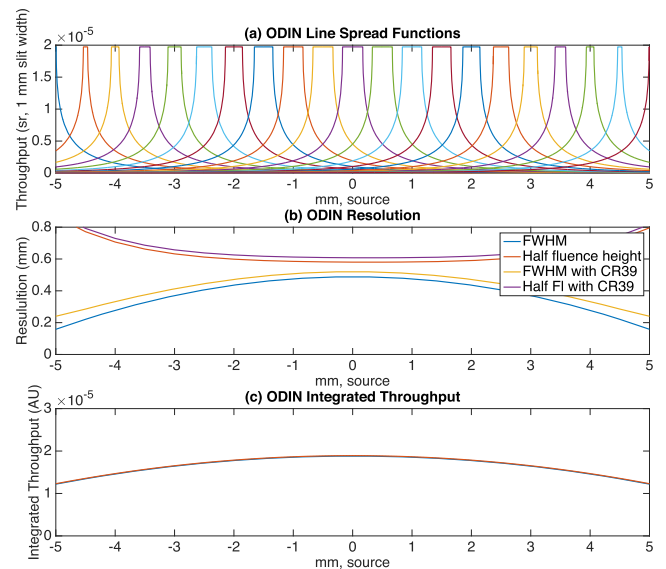
FIG. 3. Estimates of performance. (a) shows the line spread function for a 266 μm slit based on (4). (b) shows two measures of the resolution—the full width half maximum of the line-spread function and the half-fluence height; each is also shown after incorporating the CR39 resolution. (c) shows the effective throughput (acceptance angle) of the instrument.

evaluate the axial height that contains half the fluence (analogous to the half-power diameter used in x-ray optics with complicated point spread functions). Each of these metrics of resolution is shown in the figure with purely geometrically within the instrument and after incorporating the 650 μm combined resolution[16] of the HDPE-CR39 pair (due to the high magnification design, the detector resolution has a negligible contribution).

Figure 3(b) shows that with the 266-μm slit spacing, the two measures of resolution are similar on the axis and each indicates a 500-μm resolution in the source plane (20 resolving elements along the 10-mm source height). This agreement between the measures is a result of the near-Gaussian line spread function. As the source moves away from the center of the instrument, the line shape becomes less Gaussian, and the two metrics become more distinct. It is noted that the line spread function being near-Gaussian on the axis for this slit size is coincidence, for other slit spacings, this is not the case and the two measures of resolution show a greater difference over the entire field of view.

Integrating each of the line spread functions provides the effective throughput (acceptance angle) of the instrument, as shown Fig. 3(c). As can be seen, there is <50% variation in throughput across the field of view—the transmission through the W has helped flatten the throughput. This variation in throughput will affect the signal to noise levels at the edge of the field of view.

IV. DATA AND ANALYSIS

ODIN has been fielded on several MagLIF experiments. As an example, in Fig. 4, we show data from Z shot 3040, which was a MagLIF experiment that produced 4×10^{12} D-D neutron yield.[17] Multiple CR39 plates from the primary detector location in the instrument were etched in an 6N NaOH bath at 80 °C for 5 h[11] and then scanned.[12] Noise reduction techniques more aggressive than those discussed in Ref. 12 were used to reject features that are not tracks caused by incident D-D neutrons (or neutron-induced protons).

Figure 4(a) is a scan of one CR39 plate from the primary location from the MagLIF experiment. The units of the y-axis, which is the resolving direction, are millimeters in the source plane. For simplicity, we apply the same magnification to the non-resolving x axis as well. The color scale represents tracks per pixel (we have subtracted the background track density of ~2 tracks per pixel, which is evaluated from an un-exposed region of CR39). As seen in the figure, the scanned data are noisy but has some evidence of a higher track density at the mid-height of the image. This etched CR39 has been scanned at significantly higher resolution than the expected 500-μm resolution of the instrument. To optimize the signal to noise, we rebin the data closer to the instrument resolution. For experiments with lower yields, we have more aggressively rebinned the data and sacrificed some instrument resolution to enhance signal to noise. For simplicity of image processing, we rebin in both the resolving direction and the non-resolving direction. The rebinned data are shown Fig. 4(b).

Figures 4(a) and 4(b) indicate that there is variation in the track density in the vertical (resolving) direction (e.g., the bright region at y ~ −0.5 mm). Furthermore, there is correlation in the track density in the horizontal direction. Hence, within the raw data, and more so with the rebinned data, the two-dimensional scans are consistent with one-dimensional imaging.

Given than there is no information in the x direction on CR39, we can reduce the data to a one-dimensional dataset. The axially resolved track density (along the long dimension of the stagnation) shown in Fig. 5(a) is obtained by integrating each row of pixels in Fig. 4(b). Uncertainties represent the variation across the pixels that are being summed (the standard deviation in the mean, scaled to the integral). We have incorporated the axial dependence of the collection solid angle [Fig. 3(c)] and the efficiency of the CR39-HDPE pair into the unfolded neutron density. Also shown in blue in Fig. 5(a) is equivalent processing from a second layer of CR39 at the same location. Comparing the red and blue structures, we find consistency in the axial structure between the two layers.
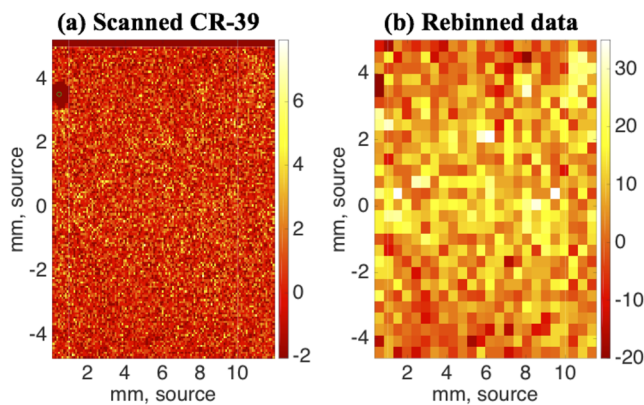

FIG. 4. CR39 track profiles from ODIN for Z shot 3040. (a) is the scanned data after correcting for instrument magnification. (b) is the same data after rebinning to the expected resolution of the instrument. The color scales on the two plots are in tracks per pixel and tracks per bin, respectively, and have had the background track density subtracted.
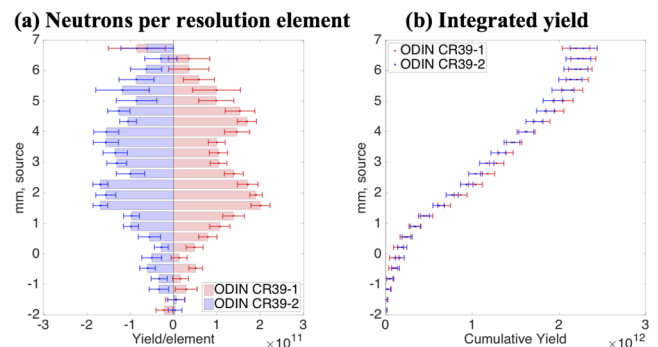

FIG. 5. (a) Comparison of the axial (vertical) structure from two different CR39 locations. The top scale shows the track density, and the lower scale shows the neutron inferred for each axial element. For clarity, the two signals are shown in different directions. Uncertainties represent the variation across each row in the two-dimensional data. (b) is the axial sum of both curves in (a).

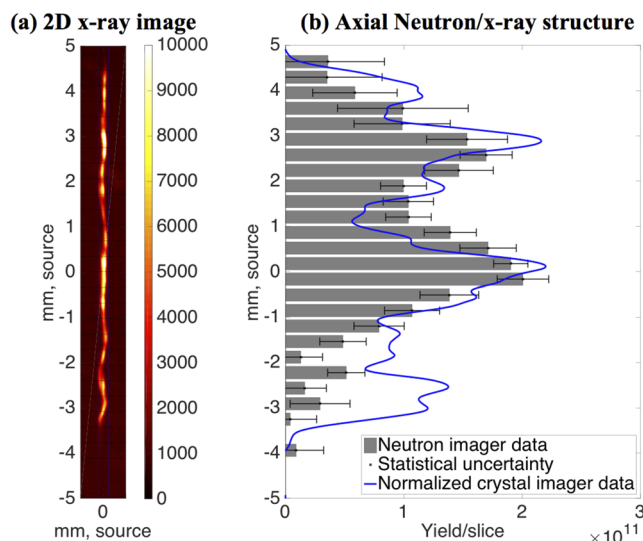**(a) 2D x-ray image**   **(b) Axial Neutron/x-ray structure**

FIG. 6. Comparison of neutron and x-ray axial structure. (a) is a monochromatic x-ray image. (b) is the axial structure from the x-ray image and ODIN (the x-ray curve is degraded to the resolution of ODIN).

By summing these tracks per axial element, we can obtain an estimate of the yield from the shot; Fig. 5(b) shows the running total of the neutrons per element. As with Fig. 5(a), the uncertainties shown represent the statistical uncertainties in the measurement and do not include other (systematic) uncertainties, which will likely be dominated by uncertainty in the efficiency of the coupled HDPE and CR39. The two CR39 layers are consistent with each other and are within a factor of two of the yield obtained from activation-based diagnostics (the use of an HDPE conversion efficiency for D-T[12] rather than D-D neutrons may explain this discrepancy). Neutron scattering corrections have not yet been applied to the imager data, which are expected to improve the yield comparisons to the activation measurements. Other experiments (not shown) have fielded the secondary/intermediate CR39 location to check consistency and as a confirmation of the correct operation of the imager. These two locations recoded consistent data.

We can compare the axially resolved neutron data to the axially resolved x-ray structure. Figure 6(a) shows a monochromatic x-ray image[6] at 6 keV for the same experiment. To compare the x-ray data to the neutron data, we reduce the two-dimensional x-ray image to a one-dimensional lineout and then blur it by the resolution of ODIN, as shown in blue in Fig. 6(b), which also shows the ODIN data. We find, for this experiment, some similarity in the axial structure of the ODIN and crystal imager data. There are some regions where the x-ray image is relatively brighter compared to the neutron

image, which could be consistent with the changes in mix or liner opacity, which will be investigated further.

V. SUMMARY

We have designed, fabricated, and fielded a one-dimensional neutron imager for the Z machine. The design was optimized for MagLIF experiments and has successfully produced one-dimensional images. In the future, we will conduct off-line D-D neutron experiments and scattering calculations to better characterize the system performance. We are modifying ODIN to incorporate a one-dimensional x-ray imager that will be co-linear to the neutron imager. The x-ray image will be produced by the same slit, and the image plate detector will be pinned ahead of CR39 in the main detector stack.

Finally, if the yields from MagLIF improve, for example, by the use of 50-50 D-T mixture, we could modify the existing instrument to either improve resolution or add 2-dimensional imaging.

[1] P. Volegov *et al.*, Rev. Sci. Instrum. **85**, 023508 (2014).
[2] D. T. Casey *et al.*, Phys. Rev. Lett. **115**, 105001 (2015).
[3] S. A. Slutz *et al.*, Phys. Plasmas **17**, 056303 (2010).
[4] A. J. Harvey-Thompson *et al.*, Phys. Rev. E **94**, 051201 (2016).
[5] P. F. Schmit *et al.*, Phys. Rev. Lett. **113**, 155004 (2014).
[6] M. R. Gomez *et al.*, Phys. Rev. Lett. **113**, 155003 (2014).
[7] G. A. Rochau *et al.*, Rev. Sci. Instrum. **70**, 549 (1999).
[8] D. N. Fittinghoff *et al.*, Rev. Sci. Instrum. **79**, 10E530 (2008).
[9] Derived from E. F. Plechaty, D. E. Cullen, R. J. Howerton, and J. R. Kimlinger, "Tabular and graphical presentation of 175 neutron group constants derived from the LLL evaluated neutron data library (ENDL)," Technical Report UCRL-50400, Lawrence Livermore National Laboratory, 1978, Vol. 16 Rev 2.
[10] For the distances used in ODIN, a 100 mm long extended slit with spacing 250 μm would provide a field of view at the load of approximately 2 mm.
[11] M. T. Collopy *et al.*, Rev. Sci. Instrum. **63**, 4892 (1992).
[12] J. A. Frenje *et al.*, Rev. Sci. Instrum. **73**, 2597 (2002).
[13] F. H. Séguin *et al.*, Rev. Sci. Instrum. **74**(2), 975 (2003).
[14] This factor of 8 is based on measurement with D-T neutrons. Experiments are planned to better quantify this D-D neutrons.
[15] J. D. Vaughan *et al.*, Rev. Sci. Instrum. **89**, 10I121 (2018).
[16] D. Fittinghoff, private communication (2018).
[17] The target was 10 mm tall, had 4.65 mm inner radius, 290 μm liner thickness with a 75 μm Epon coating for stability. Full details on this exact liner configuration will be discussed in a future publication.